Development of a Non-premixed GOx/Methane Resonance Igniter

Neeser, Jonathan; De Domenico, Francesca

DOI
10.1016/j.jaecs.2025.100392

Publication date
2025

Document Version
Final published version

Published in
Applications in Energy and Combustion Science

Applications in Energy and Combustion Science 24 (2025) 100392

Contents lists available at ScienceDirect

Applications in Energy and Combustion Science

journal homepage: www.elsevier.com/locate/jaecs

Development of a Non-premixed GOx/Methane Resonance Igniter☆,☆☆

Jonathan Neeser [a,b], Francesca De Domenico [a,*]

[a] Delft University of Technology, Faculty of Aerospace Engineering, Kluyverweg 1, Delft, 2629 HS, Netherlands
[b] Current Affiliation: Isar Aerospace SE, Caroline-Herschel-Straße 2, Ottobrunn, 85521, Germany

ARTICLE INFO

Dataset link: 10.4121/dbaa8f0f-59d2-4d58-8cc9-494af1b966f1

Keywords:
Resonance heating
Thermo-acoustic igniter
Compressible fluid dynamics
SU2
Green propellants
Non-premixed ignition

ABSTRACT

Resonance igniters are a promising alternative to conventional ignition devices for rocket engines using non-hypergolic propellants. This paper presents the development and analysis of a resonance igniter using gaseous oxygen and methane, supported by experimental measurements and numerical modelling. The effect of nozzle gap distance on acoustic resonance heating is investigated using oxygen and nitrogen as driving gases. Microphone data are used to determine the operating mode of the igniter; thermocouple data acquired on the outside of the resonator tip are used to evaluate heating performance across various nozzle pressure ratios and nozzle gap distances. A numerical model based on the open-source CFD software SU2 is developed and validated against resonance heating experimental data. This non-reacting flow model accurately captures the transition from the high-frequency Jet Screech Mode to the lower-frequency Jet Regurgitant Mode. Furthermore, it identifies the operational parameters leading to the highest rates of resonance heating observed in the experiments. Ignition attempts in non-premixed conditions, using gaseous oxygen and methane, show that the separate injection of methane in cross-flow into the combustion chamber causes severe disruption of resonance heating, preventing ignition.

1. Introduction

In the context of rocket propulsion, *green* propellants refer to combinations of fuel and oxidiser that are less toxic and less environmentally hazardous than many of the currently used storable propellants [1], such as monomethylhydrazine (MMH) and mixed oxides of nitrogen (MON). This hypergolic propellant combination is widely used in satellite propulsion systems. In 2011 hydrazine was added to the European Union candidate list of substances of very high concern through REACH (registration, evaluation, authorisation of chemicals) [2]. The high carcinogenic potential of hydrazine and its derivatives was the primary motivation. The difficulties associated with propellant handling [3] have led to an increased interest in developing less toxic alternatives [1]. Cryogenic propellants, such as liquid oxygen and methane, are being investigated as potential alternatives for long-duration space missions [4]. At the same time, orbital transfer vehicles and upper-stage propulsion systems that require multiple ignition cycles are being developed. This results in a need for highly reliable, light-weight ignition systems, capable of a high number of ignition cycles.

Thermo-acoustic igniters (sometimes referred to as *resonance* igniters) present a promising solution. Unlike a spark torch igniter, a resonance igniter does not require an external energy source (such as a spark plug) to initiate combustion. Instead, it uses the interaction between a supersonic gas flow and an acoustic cavity to bring a mixture of fuel and oxidiser above its auto-ignition temperature. The use of a thermo-acoustic igniter is advantageous for a system that requires multiple re-ignitions during a single flight. These might include the main engines of a launch vehicle, upper-stage propulsion systems, or orbital transfer vehicles. In research settings, gaseous oxygen is often used to drive acoustic resonance and can be combined with a variety of gaseous and liquid fuels, such as kerosene [5,6], hydrogen [7], or methane [8]. The use of such devices as rocket engine ignition systems has been studied since 1967 [9]. However, none have been used as flight hardware [8]. The challenge in designing a reliable resonance igniter lies in finding and maintaining an operating regime that can generate enough heat [8]. Few universal conclusions can be drawn about the resonator geometry and operating point which result in optimal heating performance. This uncertainty extends to the two main operating modes (the Jet Regurgitant and Jet Screech Mode) of the acoustic resonance and under which conditions they are initiated. There is some disagreement about which operating mode produces the highest rates of resonance heating and which is best suited for reliable ignition. While only few numerical models are able predict the switch

☆ This article is part of a Special issue entitled: 'Women in Combustion1' published in Applications in Energy and Combustion Science.
☆☆ Experimental data associated with this paper can be found at DOI: 10.4121/dbaa8f0f-59d2-4d58-8cc9-494af1b966f1.
* Corresponding author.
E-mail address: f.dedomenico@tudelft.nl (F. De Domenico).

https://doi.org/10.1016/j.jaecs.2025.100392
Received 30 June 2025; Received in revised form 12 September 2025; Accepted 14 September 2025
Available online 23 September 2025

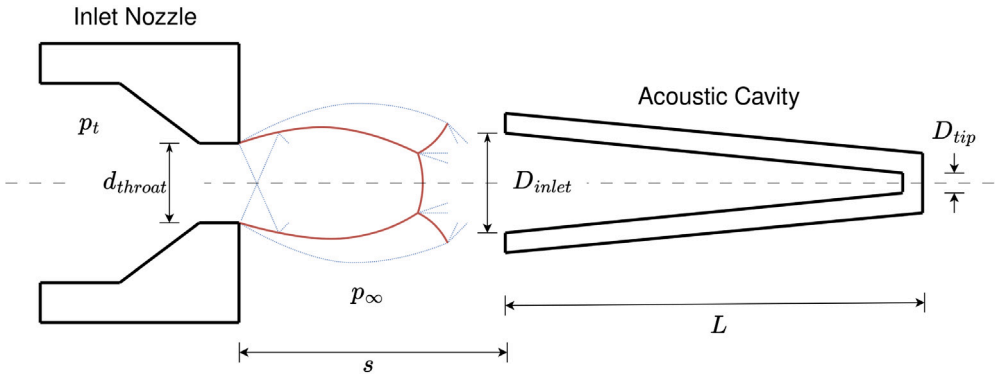

Fig. 1. Schematic of a thermo-acoustic igniter, showing the relative position of the inlet nozzle, under-expanded jet and the acoustic cavity.

in operating mode as a function of nozzle gap distance and pressure ratio [10,11], none of them seems to be able to predict the set of geometrical and operating parameters resulting in the highest rates of heat generation.

This study shows that a simplified numerical model can accurately predict the switch in operating mode, as well as the operating regime that leads to the highest rates of resonance heating. The model is validated through non-reacting experiments with a single driving gas (oxygen or nitrogen). Building on this non-reacting study, this work experimentally investigates resonance ignition with gaseous oxygen and methane in a fully non-premixed configuration. Oxygen is used as the driving gas for resonance heating and methane is injected in cross-flow relative to the shock driven oxygen flow. Owing to the lack of axisymmetry, the numerical model could not be applied to the non-premixed system. To the best of our knowledge, such a non-premixed injector configuration has not been investigated before. Most existing designs of thermo-acoustic igniters with gaseous propellants rely on premixing before injection into the resonator [7,8]. Previous studies of non-premixed gaseous injection employed a coaxial arrangement of fuel and oxidiser [12]. In contrast, this work investigates resonance ignition in a non-premixed cross-flow configuration, an approach that has so far only been attempted with liquid fuels.

This paper is organised as follows. The phenomena associated with thermo-acoustic resonance are briefly introduced in Section 2. The non-premixed resonance igniter, designed as part of this study, is described in Section 3. The numerical model, simulation parameters and the importance of using a non-ideal equation of state for these simulations, is discussed in Section 4. Results from the resonance heating experiments are shown in Section 5, including the validation of the numerical model. The results of the unsuccessful ignition experiments and their explanation are outlined in Section 6.

2. Thermo-acoustic resonance

A thermo-acoustic igniter uses the interaction between an under-expanded, supersonic gas flow and an acoustic cavity to generate heat. A combination of reversible and irreversible processes raises the temperature of the gas entrained inside the cavity [13]. Several seconds of resonance heating are typically required before the temperature at the tip of the resonance cavity can support ignition.

A schematic of a thermo-acoustic igniter is shown in Fig. 1. High-pressure gas is injected into the igniter through a choked nozzle throat with a diameter d_{throat}. The abrupt expansion after the nozzle results in a series of oblique shock- and expansion waves. Acoustic resonance can be initiated by placing a cavity at a certain distance s from this under-expanded jet.

The operating mode and the effectiveness of resonance heating primarily depend on the interaction of this under-expanded jet with the acoustic cavity. This makes the relative position of the under-expanded jet to the cavity's entrance particularly important [13]. The non-dimensional nozzle gap distance is denoted as s/d_{throat}.

The shock structure of an under-expanded jet, also shown in Fig. 1, is dictated by the ratio of total pressure in the inlet to ambient pressure surrounding the under-expanded jet, p_t/p_∞. This is commonly referred to as the Nozzle Pressure Ratio (NPR[1]). A moderately under-expanded jet features a diamond pattern of oblique shock waves. This generally occurs at $2 < \text{NPR} < 4$ [14]. If the pressure ratio increases to $4 < \text{NPR} < 7$, the jet forms a barrel structure with a Mach disk. Resonance heating has been demonstrated in weakly under-expanded gas flows but appears significantly more effective at pressure ratios above 4 [7]. In either case the shock structure and its associated pressure distribution in front of the entrance to the cavity are responsible for initiating and maintaining acoustic resonance [13].

The two most influential parameters for the interaction between the cavity and the under-expanded jet are the NPR and s/d_{throat}. Specific combinations of these parameters can trigger one of two distinct acoustic modes that produce high gas temperatures inside the cavity: the high-frequency Jet Screech Mode (JSM) or the low-frequency Jet Regurgitant Mode (JRM). These modes differ significantly in the resonance frequency and the mechanisms responsible for heat generation [13], as further elaborated in Section 4.4.

The rate of resonance heating (irrespective of operating mode) is influenced by the properties of the driving gas and the geometry of the acoustic cavity. Higher total pressure of the driving gas increases the maximum tip temperatures [8]. Similarly, gases with low molecular weight and high specific heat ratio can significantly improve resonance heating performance [15]. The use of a (semi-) conical resonance cavity, rather than a cylindrical one, also results in higher peak temperatures during resonance [5,7]. Adding a choked nozzle in the exhaust flow (after the gas has left the resonance cavity), has been shown to stabilise resonance by maintaining a constant NPR over a variety of inflow conditions [8]. Under the assumption of inviscid, ideal gas behaviour, the NPR can be expressed as the ratio of the throat and exhaust area ($NPR = A_{exhaust}/A_{throat}$) [5], as long as p_t is sufficiently high to ensure that both inlet and exhaust nozzle remain choked. A constant NPR with respect to upstream total pressure implies that the optimum s/d_{throat} also remains constant as the upstream pressure changes [8].

The propellants used in a resonance igniter are typically selected to match those of the main propulsion system to minimise complexity. Most resonance igniters use gaseous oxygen as oxidiser [5]. This can be paired with either a liquid or a gaseous fuel. With liquid fuels, such as

[1] This parameter is almost exclusively found in Western literature on the subject. By contrast, literature from countries formerly part of the Soviet-Union, use $n = p_e/p_\infty$, the ratio of static pressure in the throat of the nozzle to ambient pressure [11].

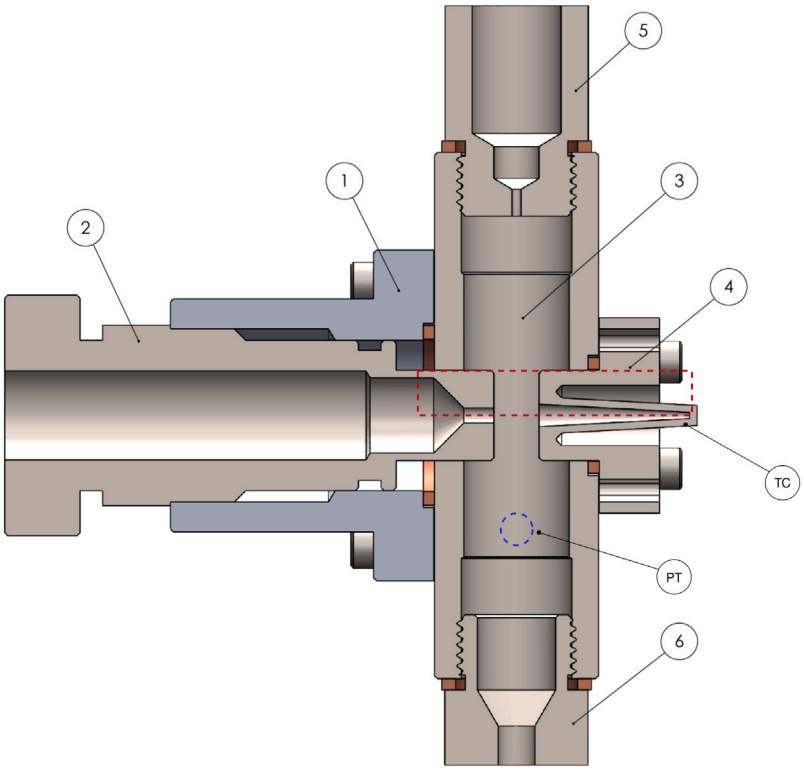

Fig. 2. Section view of the igniter assembly, (1) oxygen injector support, (2) oxygen injector, (3) combustion chamber, (4) resonator, (5) methane injector, (6) exhaust nozzle. The location of a spot welded thermocouple is indicated as TC. The port for the pressure transducer (PT) is on the opposite half of the section view. The red dashed line represents the simulation domain, described further in Section 4.

kerosene [5], or RP-1 [6], gaseous oxygen initiates resonance heating, while the fuel is injected separately into the combustion chamber. There, it mixes with the under-expanded jet and is entrained into the resonance cavity, where it can ignite. Thermo-acoustic igniters using gaseous fuels typically rely on premixing to control the mixture ratio at the tip of the resonance cavity. Successful ignition has been demonstrated under premixed conditions using gaseous hydrogen [7], and more recently using gaseous methane [8]. However, to date, ignition tests with gaseous propellants have been conducted only in premixed configurations. This work advances the current understanding by investigating the behaviour of thermo-acoustic igniters operating with non-premixed gaseous propellants, highlighting the challenges introduced by separate fuel and oxidiser injection.

3. Experimental setup

This section describes the experimental setup used for resonance heating and ignition tests with gaseous oxygen and methane. This includes the design of the resonance igniter and the propellant feed system.

3.1. Igniter design

An overview of the igniter assembly is shown in Fig. 2. Oxygen was selected as driving gas, but nitrogen was also used during commissioning experiments. The oxygen injector (2) has a d_{throat} of 2 mm (H7 tolerance). s/d_{throat} can be adjusted from 1.5 to 4 using an M24 × 1.0 thread interfacing between the injector and the injector support (1). The combustion chamber (3) serves as a mounting point for the oxygen inlet support. The main axis of the chamber is perpendicular to the resonating flow of oxygen. The fuel (gaseous methane) is injected at the top of the combustion chamber using a replaceable injection element (5). The resonator (4) is mounted to the chamber using bolts.

Table 1
Igniter design and operational parameters.

Parameter	Value	Unit
Fuel pressure	8–25	bar
Oxidiser pressure	8–25	bar
Oxidiser mass flow at 25 bar	17.73	g/s
Fuel mass flow at 25 bar	4.43	g/s
Design mixture ratio	4	–
$d_{\text{injector, O}_2}$	2	mm
$d_{\text{injector, CH}_4}$	1.2	mm
Nozzle diameter	5.2	mm
s/d_{throat}	1.5–4	–

The oxygen injector, combustion chamber, methane injector, and exhaust nozzle are manufactured from 1.4305 stainless steel. Table 1 summarises the high level design and operational parameters of the igniter. To determine an approximate mass flow rate for oxygen and methane, a discharge coefficient of 0.9 is assumed for all orifices, based on numerical results from 40° conical converging nozzles at an NPR of 6 [16].

3.2. Resonator

The conical resonator is 3D printed from 17-4 PH stainless steel using Selective Laser Melting (SLM) on an EOS M400-4. The inlet-to-throat diameter ratio D_{inlet}/d_{throat} of 1.5 is based on an optimal value found by Marchan [5]. The tip diameter of 0.8 mm, chosen as the estimated minimum printable diameter that maintains a reasonable degree of accuracy and circularity in SLM fabrication. The length of the resonance cavity is 20 mm, corresponding to a L/d_{throat} of 10. This design is similar to the resonator designed by Lungu et al. [8] and is deemed sufficiently long to initiate JRM at appropriate NPR and s/d_{throat} [13]. The resulting cone angle results in a 3.15° taper of the

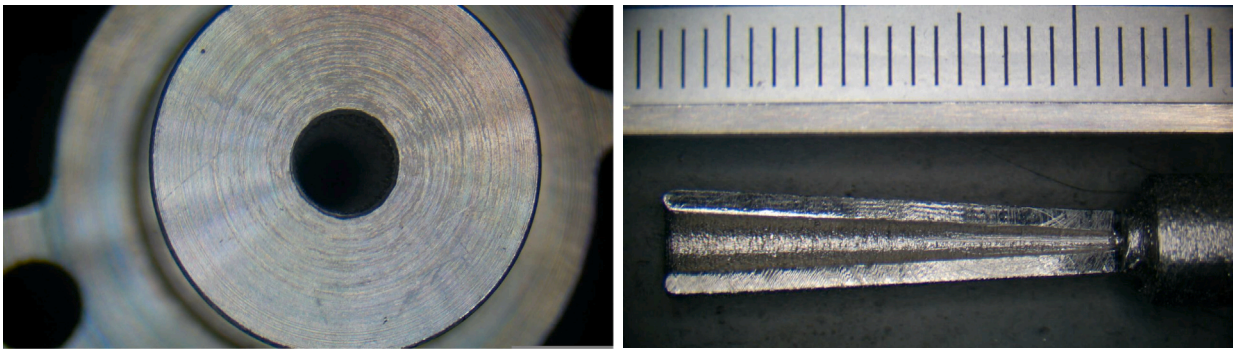

(a) Front view of the resonator inlet after post-machining. The 3 mm diameter cavity inlet is in the centre.

(b) Section view of a test print of the resonator. Note that each line in the scale represents 1 mm.

Fig. 3. Microscope images of SLM printed resonance cavity.

Table 2
Design and measured resonator dimensions.

Dimension	Design value	Measured value
Inlet diameter (mm)	3	2.83 ± 0.25
Tip diameter (mm)	0.8	0.80 ± 0.10
Resonator length (mm)	20	20.00 ± 0.18
$D_{\text{inlet}}/d_{\text{throat}}$ (–)	1.5	1.41 ± 0.125
L/d_{throat} (–)	10	10.00 ± 0.09

resonator. The interface with the chamber is post-machined to meet the required alignment tolerance. A front view of the inlet of the resonator is shown in Fig. 3(a), taken using a digital microscope.

A set of test prints was created to ensure that the SLM process properly resolved the internal dimensions of the cavity. One of these test prints is shown in Fig. 3(b). Table 2 highlights the dimensions of the resonator compared to those measured from the test print. The measured length of the cavity and the tip diameter match the design values. The inlet diameter is 6% smaller than the design value.

The expected resonance frequency of the acoustic cavity is a useful parameter for quantifying the fluid time scales for the simulations [10] and for selecting appropriate measuring equipment. The quarter wave frequency of a truncated cone f_0 can be estimated using Eq. (1) [17].

$$\frac{2\pi f_0}{a(T)} L = \pi - \arctan\left(\frac{2\pi f_0}{a(T)} L \frac{D_{tip}}{D_{inlet} - D_{tip}}\right) \tag{1}$$

where L is the length of the resonator and $a(T)$ is the speed of sound as a function of gas temperature. D_{tip} is the diameter at the resonator tip and D_{inlet} is the diameter at the entrance of the cavity. Fig. 4 shows the estimated natural frequency of the resonator as a function of gas temperature for both oxygen and nitrogen. Gas properties of oxygen and nitrogen are taken from CoolProp [18]. With the design resonator dimensions shown in Table 2, the cavity natural frequency is $f_0 = 5065$ Hz for oxygen and $f_0 = 5417$ Hz for nitrogen (at a gas temperature of 20 °C).

Based on the measurement uncertainties reported in Table 2, an error margin was added to the predicted quarter-wave frequency. The maximum upper and lower bounds of the error were determined by stacking the errors in Table 2 and identifying the permutation that causes the most significant deviation in Eq. (1). The lower bound of the error is −1.69% and the upper bound 2.56%. These error margins remain effectively constant over the temperature range shown in Fig. 4 and independent of the specific gas properties.

In addition to exciting the natural frequency of the acoustic cavity, the supersonic under-expanded jet can excite acoustic modes outside of the cavity. Notably, the volume between the under-expanded jet and the methane injector, shown in Fig. 2, could act as a Helmholtz resonator, as it does not experience through-flow during the heating phase. The neck of the resonator is the gap between the nozzle exit and the resonator inlet. Its area (A_{neck}) changes as the nozzle gap distance is adjusted, which in turn changes its natural frequency. The volume under the methane injector remains constant. The natural frequency of a Helmholtz resonator is given by Eq. (2) [19].

$$f_{0,H} = \frac{a}{2\pi}\sqrt{\frac{A_{neck}}{V_0 L_{eq}}} \tag{2}$$

Here, a is the speed of sound of the gas inside the chamber; L_{eq} the equivalent length of the neck of the Helmholtz resonator, approximated as the average vertical distance between the nozzle and the start of the combustion chamber and V_0 is the static volume inside the Helmholtz cavity. Using $s/d_{throat} = 3.5$, Eq. (2) predicts a natural frequency of 7132.5 Hz for nitrogen, and of frequency of 6664.6 Hz for oxygen. This spurious mode is observed during some experiments, as outlined in Section 5, and in some cases dominates the microphone signal over the intended operating mode of the cavity.

3.3. Piping and instrumentation

The Piping and Instrumentation Diagram (P&ID) for the final fluid system is shown in Fig. 5, including operational pressures, gases and sensors. Three solenoid valves are used to control the flow of oxygen, methane, and nitrogen. Check valves are placed on both the fuel and oxidiser lines upstream of the igniter to prevent reverse flow. Gas cylinder supply pressure is regulated using manually set diaphragm regulators. The nitrogen purge is only supplied through the fuel line, preventing the purge gas from causing unintentional resonance heating. Note that the line to the methane cylinder is only added for combustion tests.

Two K-type thermocouples (TC) are spot welded to the tip of the resonator to sample the temperature of the outer wall at 100 Hz. Pressure transducers ifm PT5423 (PT) are placed upstream of the oxygen and methane injectors and in the combustion chamber and sampled at 2.5 kHz. The chamber pressure transducer is separated from combustion gases using a stand-off pipe. In order to capture the expected resonance frequency of the acoustic cavity in both JRM and JSM, a microphone is placed outside of the resonator (ICP Microphone from PCB, 100 kHz sampling rate), providing a non-invasive measurement of the acoustic resonance.

4. Simulation setup

The numerical model presented in this study uses the open-source CFD software SU2 [20] to simulate resonance heating in resonance igniters. This non-reacting simulation demonstrates that a simplified 2D axis-symmetric model can predict the switch between operating modes

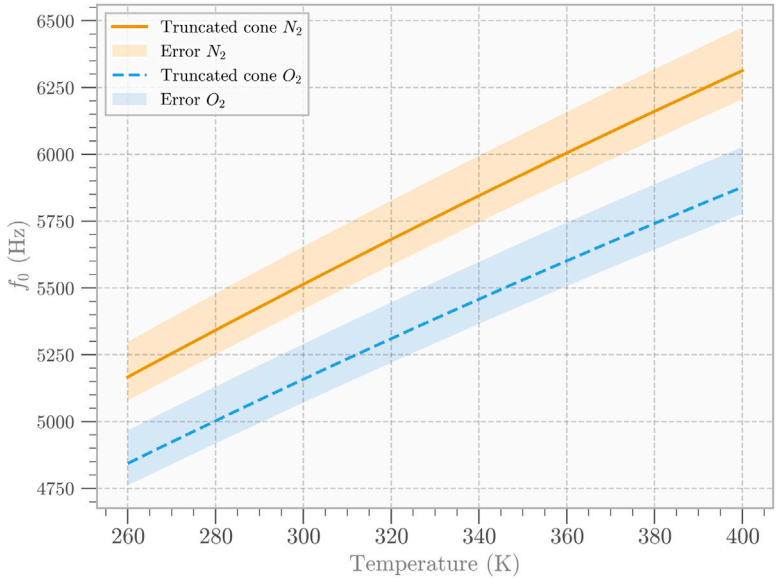

Fig. 4. Quarter-wave resonance frequencies of oxygen and nitrogen as a function of temperature for the truncated cone resonator geometry used in this study.

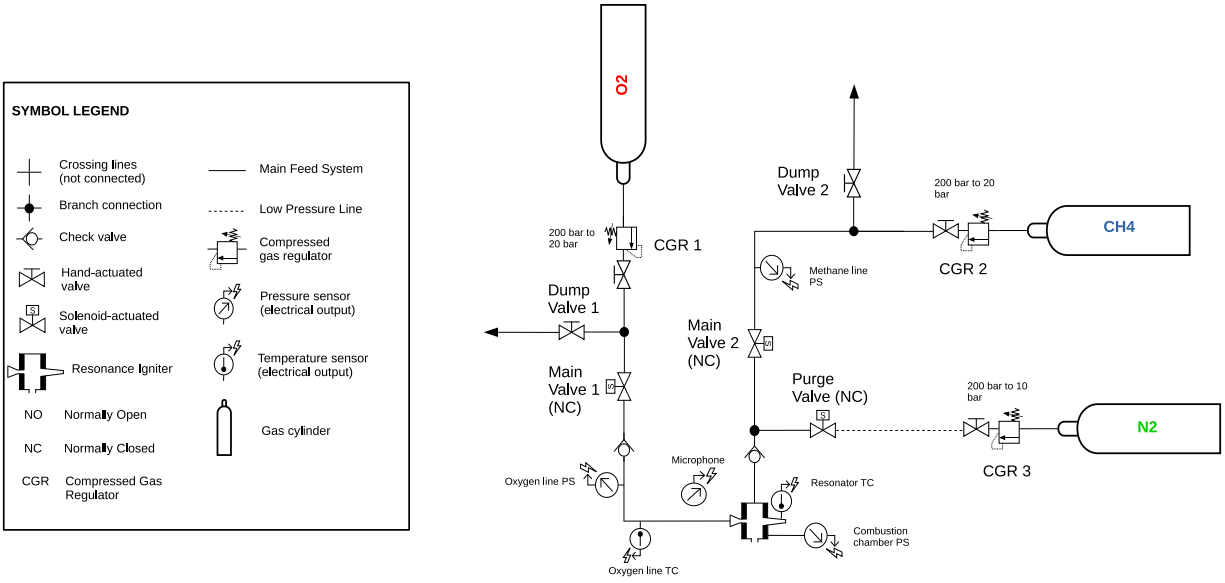

Fig. 5. P&ID of the propellant feed system.

during the heating phase and can therefore be used as part of the igniter design process. The simulations use an Unsteady Reynolds-Averaged Navier–Stokes (URANS) approach with k-ω SST turbulence model and incorporate a non-ideal gas model. Extensive validation of the model is performed using the experimental data acquired varying nozzle gap spacing,using both oxygen and nitrogen as driving gases, as detailed in Section 5. Only the part of the flow associated with the driving gas and the resulting shock system is approximately axisymmetric (See the red box in Fig. 2), and this is the region represented in the 2D model. The injection of methane, perpendicular to the driving gas, is not simulated in this study, since the non-premixed cross-flow injection configuration breaks the assumption of axisymmetry and would require a fully three-dimensional model, outside the scope of this study.

The Peng–Robinson–Stryjek–Vera equation of state (EOS) [21] is used for the coupling between density and pressure, as well as for determining the specific heat capacity of the driving gas. These properties are relevant for predicting the heat transfer to the cavity wall and for capturing the temperature rise across the incident and reflected shock waves [22]. The flow inside the resonator experiences temperatures below 170 K during the outflow phase of JRM and close to 100 K inside the under-expanded jet. Under these conditions, the more accurate pressure–density coupling of the cubic EOS offers a better prediction of the pressure distribution upstream of the resonance cavity, which are critical for initiating the next inflow cycle [23]. The pressure field during the outflow determines both the uniformity and the energy of the subsequent inflow event. The temperature-dependent viscosity of the gas is modelled using Sutherland's law. A constant turbulent and laminar Prandtl number are assumed, leading to a temperature-dependent value for thermal conductivity.

4.1. Simulation domain and boundary conditions

An illustration of the computational domain is shown in Fig. 6(a), and highlighted in Fig. 2. It includes the converging section of the oxygen inlet, the gap spacing between the nozzle and the resonator, the resonance cavity, and the outlet. A structured mesh is used throughout

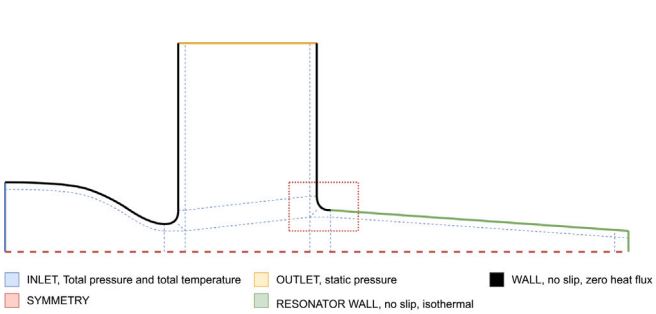

(a) Schematic of the computational domain and boundary conditions. Note that the corner radii are not to scale.

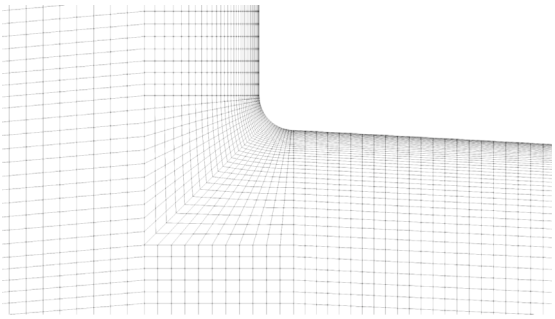

(b) Visualisation of a critical mesh region at resonator inlet at 75% of the nominal number of nodes (for visual clarity), corresponding to the dashed rectangle in Figure 6a.

Fig. 6. Critical mesh regions and boundary conditions.

the domain, with local boundary layer refinement. The domain comprises approximately 96,000 mesh elements, of which 45 000 elements are allocated to the resonance cavity. A time average $y^+ < 1$ is achieved along the entire resonator wall. Approximately 4–5 mesh elements are placed within $y^+ = 5$ to ensure appropriate near-wall resolution. Fig. 6(b) shows a detailed view of the mesh at the inlet of the resonance cavity. A rounded corner with radius $r = 0.03 \cdot d_{throat}$ is artificially applied to the resonator inlet and the nozzle outlet to improve numerical stability by avoiding high aspect ratio orthogonal cells at the intersection of the resonator and outlet.

The simulation domain is symmetric around the x-axis. The inlet boundary condition prescribes the total pressure and temperature of the driving gas, allowing to match the simulated inlet conditions to experimental measurements. Static pressure is prescribed at the outlet, where the length of the outlet is set to five times the throat diameter to ensure sufficient distance from the under-expanded jet. The wall of the resonance cavity is assumed to behave as an isothermal, no-slip wall, while all other walls in the domain are also no-slip but adiabatic. While the use of an isothermal wall was found to improve the stability of the simulation, compared to setting a constant heat transfer coefficient, this assumption introduces two sources of error compared to the experiments. Fixing the wall at ambient temperature results in higher predicted heat flux at the tip of the resonance cavity. Furthermore, a higher outward heat flux also means that the gas temperature inside the resonator is lower in the simulation than in the experiment, which affects the predicted resonance frequency, as the local fluid temperature influences the speed of sound in the cavity. As shown in Section 6, an increase in resonator tip temperature of 457.4 K causes an increase in the cavity natural frequency of 62 Hz. This observed shift in f_0 constitutes the upper bound of the frequency error due the assumption of a constant wall temperature.

4.2. Time scales

The two primary physical phenomena of interest in resonance heating are the temperature rise of the gas inside the resonator and the heat transfer through the resonator wall. The flow and the conductive time scales are given by Eq. (3).

$$\tau_{flow} = \frac{1}{f_0} \quad , \quad \tau_{cond} = \frac{L^2}{\alpha} \tag{3}$$

Here, f_0 is the natural frequency of the resonance cavity; L is a length scale (in this case, the wall thickness of the resonator), and α is the thermal diffusivity of the material. Experimental results show a cavity natural frequency of around 4900 Hz for oxygen (as shown in Fig. 12), which matches the predicted frequency from Eq. (1). The corresponding flow time scale is $\tau_{flow} = 2.04 \cdot 10^{-4}$ s. The resonator wall is 1 mm thick and made from 17-4 PH stainless steel, with a thermal diffusivity of $5 \cdot 10^{-6}$ m^2/s, resulting in a conductive time scale of $\tau_{cond} = 0.2$ s. This means that the time scale associated with a change in wall temperature is three orders of magnitude slower than the time scale of the acoustic phenomena.

The simulations used to assess the heating performance at different s/d_{throat} cover a total of $2 \cdot 10^{-3}$ s of flow time. This means that the temperature of the resonator wall is expected to change very little over the course of one of these simulations. The assumption of a constant wall temperature is justified by the simulation time being two orders of magnitude shorter than the conductive time scale of the resonator wall. In Section 5.3 the simulated heat flux through the tip of the resonance cavity is used instead of the tip temperature to evaluate the heating performance of the cavity at specific s/d_{throat}.

4.3. Solver setup

In an unsteady simulation of resonance heating, the gradients in velocity, pressure, and temperature are very high throughout the flow field. The flow inside the resonance cavity periodically experiences reverse flow inside the boundary layer. This occurs as the reflected shock wave collides with flow moving towards the cavity tip. As a result, a high degree of numerical dissipation is required to stabilise the simulation.

SU2 solves the unsteady RANS equations through a finite volume discretisation. The presence of shock waves necessitates special treatment of the convective terms in the RANS equations. A density-based solver with a classical Roe scheme [24] is employed for determining convective fluxes. A first-order upwind scheme offers excellent numerical stability over all possible operating regimes at the expense of introducing a significant degree of numerical diffusion. The use of a higher-order convective scheme would provide a better estimate of the pressure and temperature at the tip of the cavity (for a given number of mesh elements). Second order MUSCL reconstruction was tested, but lead to significant instabilities. Slope limiters based on methods by Venkatakrishnan and Wang [25] did not provide sufficient improvement. Verification using a mesh refinement study based on a grid convergence index and Richardson extrapolation, shown in Appendix B, demonstrates low sensitivity of the flow density to mesh resolution.

Gradient reconstruction from the cell centre is accomplished using the Green-Gauss node-based method. The effect of turbulence is modelled using the 2003 iteration of the k-ω SST turbulence model [26]. This model performs well under adverse pressure gradients [27], a condition encountered both near the resonance cavity inlet and along the cavity wall.

The Courant–Friedrichs–Lewy (CFL) condition puts a stability limit on the largest time step possible for a given time integration scheme. For high flow velocities and fine grid sizes, the CFL condition forces

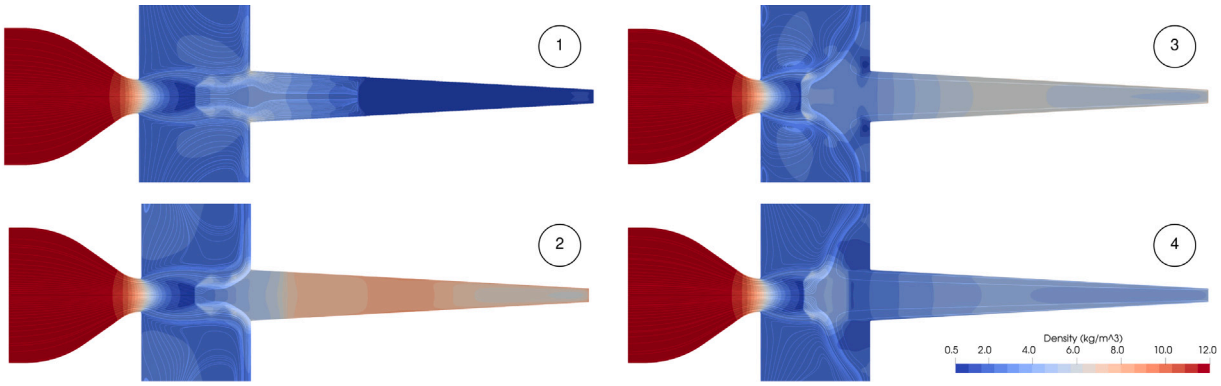

Fig. 7. Simulated flow cycle in JRM, showing density and velocity streamlines, taken at s/d_{throat} = 3.25 and NPR = 6.8. (1) beginning of the inflow phase with a shock wave moving into the resonance cavity. (2) and (3) transitional phases, as first the reflected shock wave leaves, followed by the Mach disk reaching its closest point to the nozzle. (4) end of the outflow phase, just before the start of the next flow cycle.

a very small time step on explicit time integration schemes [28]. This necessitates a very high number of iterations and high computational cost. The time step can be increased significantly using a second-order-accurate dual-time stepping method with implicit time integration. In this work, a quasi-steady state problem is solved between each time step, which leads to a higher computational cost per time step but allows for significantly larger time steps [10]. Using this technique, a time step of $4 \cdot 10^{-8}$ s proved sufficient for numerical stability and adequate shock resolution.

4.4. Description of operating modes

The numerical model was used to conduct an extensive range of resonance heating simulations. These simulations successfully replicated the experimental parametric sweeps across different s/d_{throat} using either nitrogen or oxygen. The total inflow conditions and the static outflow pressure were set according to the values measured during the corresponding experiments.

For the parametric sweeps over different s/d_{throat}, each simulation was run for $5 \cdot 10^4$ time steps (corresponding to 2 ms of actual flow time). A startup transient of two flow cycles (corresponding to $1 \cdot 10^4$ time steps) was excluded from the analysis. Selected cases, namely for s/d_{throat} = 1.5, 2, 2.05, 3 for nitrogen and s/d_{throat} = 3 for oxygen were simulated for a total of $2 \cdot 10^5$ time steps to enable a more accurate comparison between simulated and experimental pressure spectra. The results of these simulations, including validation with experimental data, are presented in Section 5.

The parametric sweep over s/d_{throat} allows for a detailed analysis of JRM and JSM as observed in both simulations and experiments. A complete flow cycle of JRM is shown in Fig. 7, simulated at s/d_{throat} = 3.25 and NPR = 6.8 using nitrogen. The flow patterns show good agreement with the results of Sarohia and Back [13] and Sobieraj and Szumowski [29], obtained using Schlieren imaging.

The Jet Regurgitant Mode consists of four stages that repeat cyclically, with a cycle period closely matching the quarter wave frequency of the cavity [13,30]. During the *inflow phase*, image (1), the pressure inside the resonance cavity is low, allowing the under-expanded jet to push gas into the cavity in the form pressure waves. If the L/d_{throat} is sufficiently large, these pressure waves can coalesce into a single shock wave [13], which reflects off the tip of the cavity and travels back towards the nozzle. The incident and reflected shock wave are primarily responsible for the increase in temperature and pressure at the tip of the cavity. The inflow entering the cavity also causes the gas entrained at the tip to be compressed, further increasing temperature and pressure. Friction between the entrained gas and the cavity wall also causes a temperature rise. Brocher and Maresca note that for low pressure ratios the dissipation of mechanical energy through friction can contribute up to 50% to the total heat generation [31]. At higher pressure ratios the shock heating becomes the more dominant mechanism. The relative importance of the two depends on several factors, including cavity length, cavity shape and surface roughness. After leaving the cavity, the shock wave induces a series of expansion waves that propagate towards the tip of the cavity. The *transitional phases*, images (2) and (3), mark a low-pressure region in the wake of this expansion wave, that results in fluid leaving the cavity. The flow leaving the cavity pushes the Mach disk of the under-expanded jet rearward. Eventually, the interface between the outflow from the cavity and the under-expanded jet comes to a standstill. The *outflow phase* concludes when this reflected expansion wave exits the cavity, as shown in image (4). As the low pressure behind the reflected expansion wave reaches the cavity inlet, the interface between the under-expanded jet and the outflow from the cavity is suddenly weakened. The Mach disk can again move towards the cavity inlet allowing the next inflow cycle to begin.

The Jet Screech Mode typically occurs when the cavity is placed at s/d_{throat} smaller than the length of the first shock structure of the under-expanded jet [13]. Schlieren images show a strong bow shock forming in front of the entrance to the cavity, completely encompassing it. This bow shock acts like a dynamic membrane weakly compressing and expanding the gas inside the resonance cavity [13,29]. Visualisation of a complete flow cycle of JSM is shown in Fig. 8, simulated at s/d_{throat} = 2 and NPR = 6.8 using nitrogen. During each bow shock oscillation, weak pressure waves travel down the length of the cavity, as shown in images (1) and (2). Unlike in JRM, multiple compression waves enter the cavity before the first one is reflected off the cavity's end-wall. Little to no fluid leaves the cavity during these oscillations as the pressure difference experienced by the gas inside the cavity is significantly lower than during JRM. The cumulative effect of wave-induced friction with the cavity wall gradually increases the temperature of the entrained gas. Only minimal movement of the Mach disk is observed during the various compression and expansion cycles.

5. Resonance heating results: Experimental and numerical investigations

This section presents results from 95 resonance heating experiments, demonstrating the influence of the nozzle gap spacing on the operating mode of the igniter and on the maximum tip temperature. The switch from JSM to JRM is captured both experimentally and numerically. The predictive accuracy of the simulation for predicting the resonance heating is discussed in Section 5.2, while the associated thermal effects are outlined in Section 5.3.

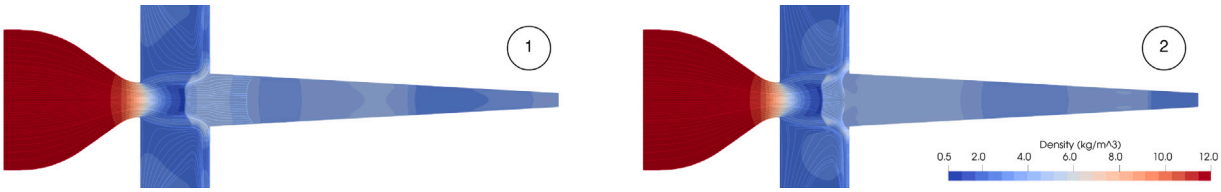

Fig. 8. Simulated flow cycle in JSM, showing density and velocity streamlines, taken at s/d_{throat} = 2 and NPR = 6.8. (1) Shows a pressure wave entering, (2) shows this pressure wave reflected, while another is entering the cavity. The interval between (1) and (2) represents the full movement of the Mach disk.

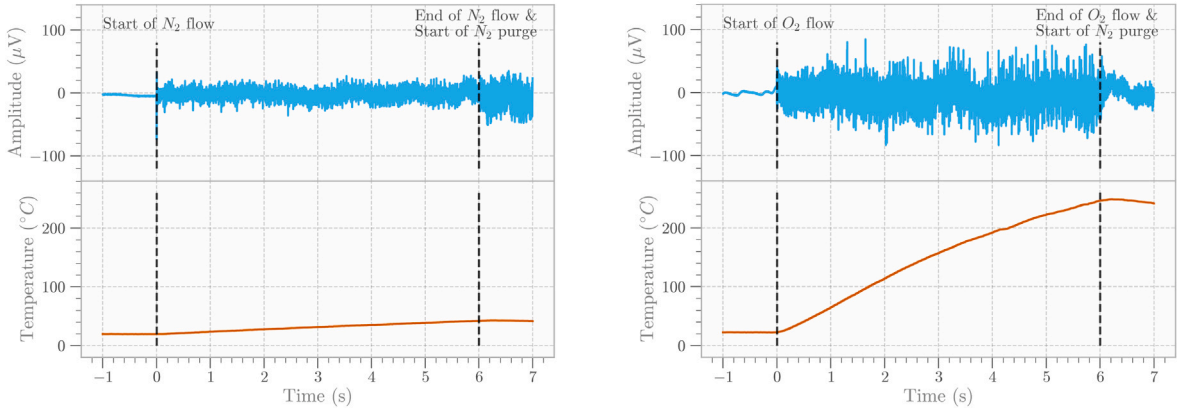

(a) Cavity operating in JSM using nitrogen. Corresponding spectrum shown in Figure 11a

(b) Cavity operating in JRM using oxygen. Corresponding spectrum shown in Figure 12a

Fig. 9. Sound pressure trace (top) and tip temperature (bottom) from resonance heating experiments.

5.1. Experimental results

During the heating tests the nozzle gap spacing (s/d_{throat}) was varied between 1.5 and 4 for nitrogen, while a narrower parametric sweep was conducted with oxygen, between 2.5 and 3.5, due to limited supply of the gas. Each set point was tested between three and eight times to confirm the consistency of the microphone spectra and tip temperature. The initial tests used six seconds of resonance heating, followed by a short nitrogen purge, as shown in Fig. 9, which displays the microphone and thermocouple signals acquired during tests in a JSM mode (a) and JRM mode (b). The selected heating time allowed for a significant temperature rise, but not for the tip temperature to reach steady state. Steady-state conditions were typically reached only after 18 s (as verified with nitrogen at select s/d_{throat}).

Two thermocouples were used to measure the temperature outside the cavity. They were spot welded between $x/L = 0.9$ and $x/L = 1.0$, representing the location of the expected maximum temperature [31]. The measured temperature was later corrected for the response time of the thermocouple, using the methodology outlined by [32]. This correction is particularly relevant for the rapid initial temperature rise, given the thermocouples' estimated response time of $\tau = 0.1$ s.

The microphone placed outside of the cavity was used to investigate the acoustic resonance within the cavity. The time interval between T+1 and T+5 s was selected for spectral analysis, resulting in a total of $4 \cdot 10^5$ samples used for the fast Fourier transform (FFT) of the microphone signal. The resulting spectra were used to identify the dominant acoustic mode corresponding to each operating condition.

Figs. 10(a) and 10(b) show the spectra of the pressure trace with varying s/d_{throat} using nitrogen and oxygen as driving gases respectively. It should be noted that the NPR differs slightly between the two sets, as the manually adjusted gas regulators used in the experiments introduced some variation in the upstream pressure. Specifically, the nitrogen tests were conducted at NPR = 6.8, while the oxygen tests at NPR = 6.4. All spectra are normalised to the maximum amplitude measured with each driving gas.

Fig. 10(a) shows a clear onset of a Jet Regurgitant Mode at s/d_{throat} = 2., which is the lowest nozzle gap distance at which the fundamental frequency of the cavity has the highest amplitude in the spectrum. This is accompanied by a noticeable increase in tip temperature, as discussed in Section 5.3. The cavity operates in JRM up to and including s/d_{throat} = 4. The fundamental frequency and its first two overtones are the highest in the spectrum at s/d_{throat} = 3, which is the point of maximum tip temperature. Conversely, at s/d_{throat} = 1.5, no distinct peaks are visible in the spectrum below 24 kHz, and the heating effect is negligible. At this gap spacing, the highest amplitude occurs around 40 kHz, indicating a Jet Screech Mode.

A sudden shift in the dominant frequency, from 5306 Hz to 7026 Hz, is observed between s/d_{throat} = 3.25 and s/d_{throat} = 3.5, as shown in Fig. 10(a). The dominant frequency returns to 5644 Hz at s/d_{throat} = 4. The shift results from a secondary resonance mode excited at that particular gap spacing. Specifically, the volume between the main flow axis through the nozzle and the methane injector forms a cavity resembling a Helmholtz resonator, whose resonant frequency is predicted to be 7132.5 Hz by Eq. (2). To test this hypothesis, the resonator was mounted on an alternative mount with four exhaust holes arranged around the flow axis of the resonating gas. With this configuration, f_0 remains around 5500 Hz at s/d_{throat} = 3.5, indicating that the microphone, when the system was mounted inside the combustion chamber at s/d_{throat} = 3.5, detects the Helmholtz frequency $f_{0,H}$ instead of the natural frequency of the cavity. The same shift in f_0 is observable in Fig. 10(b) at s/d_{throat} = 3.25, where the natural frequency increases from 4882 Hz to 6674 Hz. The lower speed of sound of oxygen could cause the onset of the same secondary resonance at a slightly lower gap spacing than that for nitrogen.

Fig. 10(b) shows that between s/d_{throat} = 2.5 and s/d_{throat} = 3.5 the cavity appears to be operating in JRM when using oxygen. The results shown in Fig. 10 differ notably from results obtained by Lungu et al. [8]. Lungu et al. observe a clear onset of JRM only at s/d_{throat} = 3.5 when using oxygen, at an NPR of 6.31. Closer agreement is found with results from Sarohia and Back, who predict an onset of

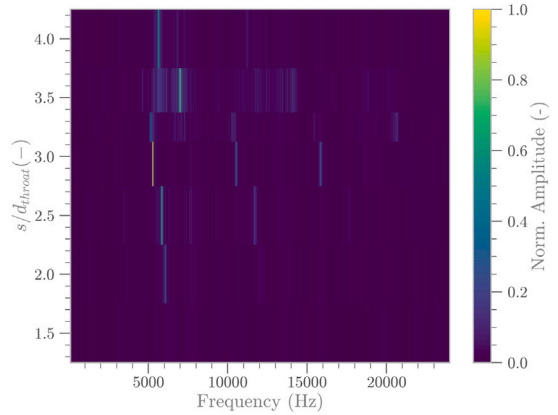

(a) Frequency spectrum for different s/d_{throat} for nitrogen with NPR = 6.8.

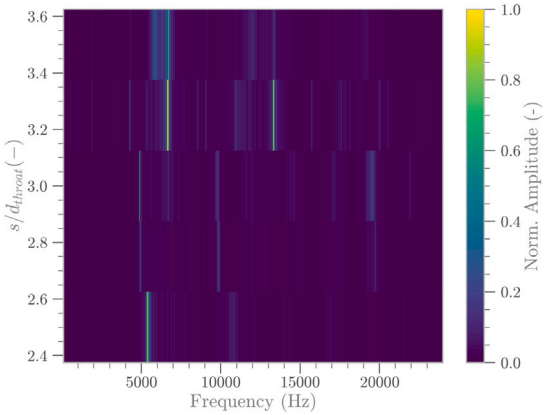

(b) Frequency spectrum for different s/d_{throat} for oxygen with NPR = 6.4.

Fig. 10. Spectra of parametric sweeps with oxygen and nitrogen.

JRM near s/d_{throat} = 2.5 for NPR = 6.8 when using nitrogen [13]. Important differences exist between the resonance cavities used for these experiments and those tested by the other authors [8,13]. While the cavity shape and size are quite comparable, Lungu et al. used a sharp-edged inlet to the resonance cavity, as opposed to the blunt inlet used in the experiments described in this work. Sarohia and Back used a conical resonance cavity with a significantly lower L/d_{throat} to characterise this specific combination of s/d_{throat} and NPR.

5.2. Validation of the numerical model against experimental results

The validation of the CFD simulations is carried out by comparing the simulated natural frequency of the resonance cavity at selected nozzle gap distances with the corresponding experimental data. The simulated spectra are extracted from the pressure on the centreline of the resonator, at x/L = 0.99. This location was chosen as it lies in the region of the resonator of maximum pressure fluctuations, while remaining outside of the boundary layer at the cavity tip. Fig. 11(a) shows a comparison between simulated and experimental spectra of the cavity operating in JSM, while Fig. 11(b) shows the first occurrence of JRM.

At s/d_{throat} = 1.5 the cavity operates in a Jet Screech Mode (JSM). Fig. 11(a) shows that the simulation at the same nozzle gap distance successfully reproduces this operating mode. A simulation run at s/d_{throat} = 1.55 features a dominant frequency within 3.79% of the experimental results. The onset of a clear Jet Regurgitant Mode is experimentally observed at s/d_{throat} = 2. The simulation at this gap spacing shows a transitional mode between JRM and JSM, with a prominent peak near the natural frequency of the cavity, as well as a peak near 30 kHz. A similar superposition of the two modes has also been reported by Bauer et al. [33]. The simulation predicts the actual onset of JRM at s/d_{throat} = 2.05, with an error in the natural frequency of only 2.59%. The first overtone of the natural frequency is also clearly visible in the simulated spectrum.

A comparison of Figs. 11(b) and 12(b) shows that the simulation accurately reproduces the shift in fundamental frequency between s/d_{throat} = 2 and s/d_{throat} = 3 from 6252 Hz to 5558 Hz observed experimentally for nitrogen. During the inflow phase at s/d_{throat} = 2.05 (JRM) the simulation shows two shock waves entering the cavity, separated by approximately 0.029 ms. These two shock waves appear weaker than the single shock wave entering the cavity at $s/d_{throat} \geq 2.5$. During the outflow phase at s/d_{throat} = 2.05, the simulation indicates that these two shock waves impart less momentum to the under-expanded jet, compared to other gap distances. This results in less motion of the Mach disk as the flow exiting the cavity pushes the under-expanded jet towards the nozzle. Consequently, the transition to the next inflow phase occurs sooner, shortening the period of a single JRM cycle.

Table 3
Validation of the accuracy and precision of the simulation against the experiment.

Gas	s/d_{throat} Experiment (–)	s/d_{throat} Simulation (–)	f_0 error (%)
N_2	1.5 ± 0.028	1.5	11.32
N_2	1.5 ± 0.028	1.55	3.79
N_2	2.0 ± 0.028	2.0	9.43
N_2	2.0 ± 0.028	2.03	6.57
N_2	2.0 ± 0.028	2.05	2.59
N_2	3.0 ± 0.028	3.0	4.62
O_2	3.0 ± 0.028	3.0	5.23

Figs. 12(a) and 12(b) compare the simulated and experimental spectra at s/d_{throat} = 3 using oxygen and nitrogen respectively. The simulated and experimental spectra show close agreement at s/d_{throat} = 3 using nitrogen. The experimentally obtained spectrum clearly displays the natural frequency of the resonance cavity and its first two overtones, with an error in the predicted natural frequency of 4.62%. In Fig. 12(b) the fourth overtone is barely visible around 26 200 Hz in the experimental data, while the simulation shows several additional integer multiples of the first harmonic (with decreasing amplitude). As the experimental measurements were obtained using a microphone placed several centimetres away from the resonance cavity, it is possible that some of the higher-order modes were attenuated by sound travelling through the resonator wall.

Using oxygen as the driving gas, the first harmonic of the cavity is over-predicted by 5.23%, as shown in Fig. 12(a). The locations of the first three overtones of this natural frequency are clearly visible in both the experimental and numerical results. The experimental data show an additional peak around 6800 Hz and its overtones up to 32 kHz, which are not visible in the simulation. This peak is likely related to the secondary resonance observed at s/d_{throat} = 3.5. The 2D axis-symmetric simulation cannot capture interactions between the under-expanded jet and parts of the combustion chamber. A summary of the accuracy and precision of the model for all cases is shown in Table 3. These represent all simulations run for $2{\cdot}10^5$ time steps and for which detailed spectra could be generated. Simulations cases at s/d_{throat} = 2, 2.03 and 2.05 are shown. These intermediate steps around the onset of JRM are used to show the convergence of the frequency error as the simulation approaches s/d_{throat} = 2.05.

Overall, the simulation is able to accurately predict the resonance frequencies and the onset of JRM. For the transition from JSM to JRM, a small offset in nozzle gap distance of 2.5% is required for the simulation

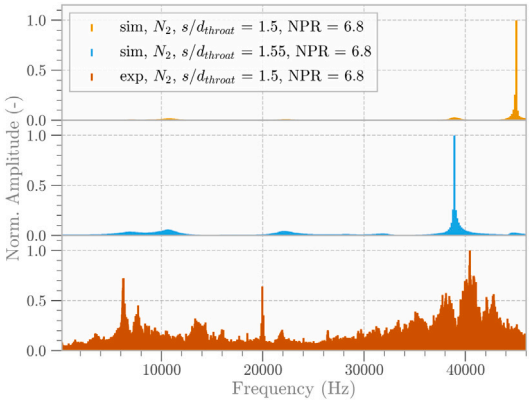

(a) Comparison of simulated spectrum at $s/d_{throat} = 1.5$ and 1.55, with experimental spectrum for $s/d_{throat} = 1.5$. All three spectra show JSM

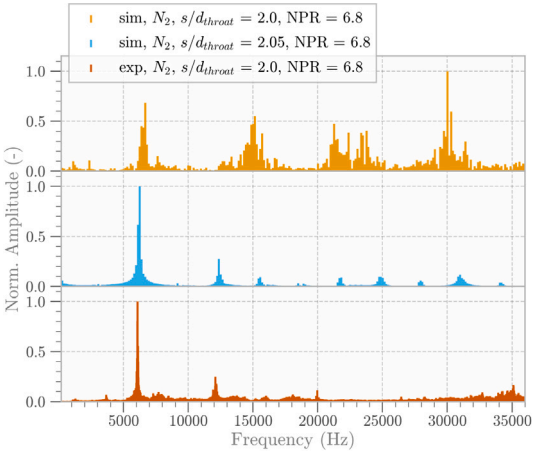

(b) Comparison of simulated spectrum at $s/d_{throat} = 2.0$ and 2.05, with experimental spectrum for $s/d_{throat} = 2.0$. The experimental results at $s/d_{throat} = 2.0$ and the simulated spectrum at $s/d_{throat} = 2.05$ show clear JRM. Meanwhile the simulated spectrum at $s/d_{throat} = 2.0$ shows a transitional mode.

Fig. 11. Model validation for the transition between JSM and JRM using nitrogen.

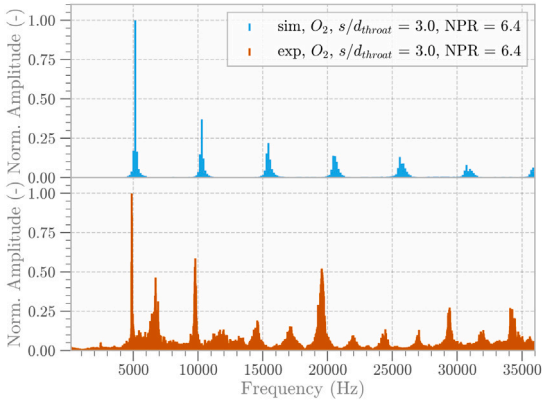

(a) Comparison of simulated and experimental spectra at $s/d_{throat} = 3$, using oxygen.

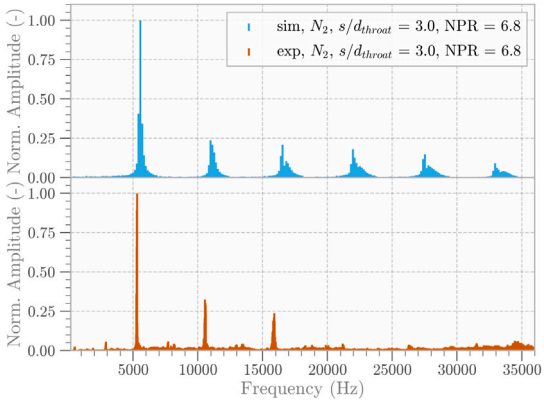

(b) Comparison of simulated and experimental spectra at $s/d_{throat} = 3$, using nitrogen.

Fig. 12. Model validation at $s/d_{throat} = 3$, using different gases.

to fully capture the operating mode observed experimentally. The exact cause of the delay in the onset of JRM in the simulated spectra requires further investigation. The discrepancy in nozzle gap spacing can be partially attributed to the uncertainty in evaluating s/d_{throat}, as the nozzle gap distance was manually adjusted between experiments using a screw thread, resulting in an estimated error of $\Delta s/d_{throat} = 0.028$. Deviations from the expected cavity shape in the SLM printed resonator can produce errors in the predicted frequency between −1.69% and 2.56%, as shown in Section 3.2.

Another source of discrepancy between the numerical model and the experimental setup is the discharge coefficient of the injector, which accounts for viscous effects reducing the effective throat diameter. The C_d of the nozzle predicted by the simulation is 0.96, however the discharge coefficient of the injector used in the experiment is expected to be lower, as a result of sharp edges in the converging section and surface roughness. The reduction in effective throat diameter increases the effective s/d_{throat}. Since a mass flow meter was not present in this experimental setup, this error could not be quantified.

As demonstrated in Section 5.3, these simulations are also able to predict the parameters that lead to the highest rates of heat generation. In the case of oxygen, both simulation and experiment show lower heating performance across all nozzle gap distances. The maximum simulated heating power using oxygen is 11.3% lower than the maximum value attained with nitrogen, while the maximum temperature differs by 10.8%.

A clear maximum in total heating power is predicted for nitrogen at $s/d_{throat} = 3$, matching experimental results exactly. In the case of oxygen, the point of maximum heat generation deviates from the experimental data: the simulation predicts the maximum heating power at $s/d_{throat} = 3.25$, as opposed to $s/d_{throat} = 2.75$ observed experimentally.

Despite these mismatches, the simulations predict the experimentally observed heat flux trends quite well and accurately capture the relative differences in heating performance across nozzle gap distances. The simulations reproduces the behaviour of both the JRM and JSM. These results demonstrate that, while minor discrepancies remain, the numerical model provides a reliable tool for predicting resonance-driven heating and guiding the design of future igniter configurations.

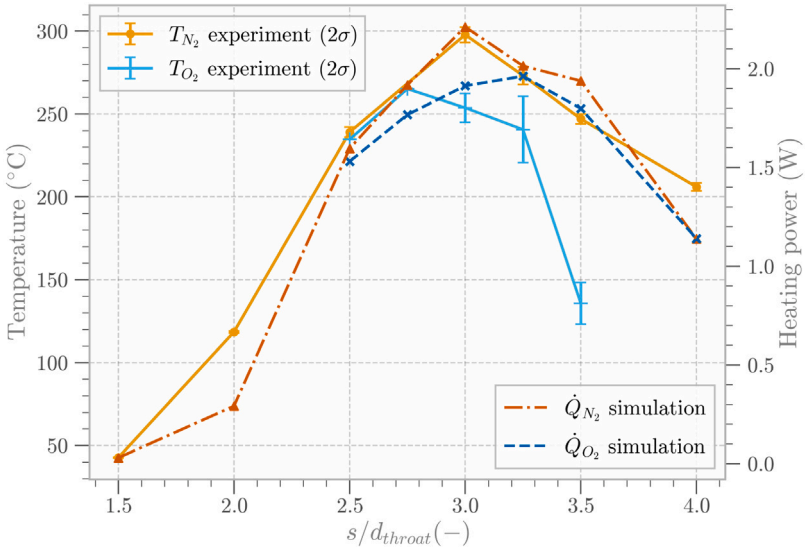

Fig. 13. Experimental maximum tip temperatures measured after 6 s of resonance heating. Between three and nine tests were conducted per s/d_{throat} set point. Compared to simulated heating power.

5.3. Tip temperature and heat flux

The maximum tip temperature as a function of nozzle gap spacing is shown in Fig. 13. The onset of JRM, identified at $s/d_{throat} = 2$, is also accompanied by a significant increase in tip temperature. The maximum temperature for nitrogen is observed at $s/d_{throat} = 3$. For oxygen, this maximum occurs at $s/d_{throat} = 2.75$ instead, and is significantly less pronounced compared to nitrogen. At larger nozzle gap distances, the tip temperature decreases rapidly, even though the igniter still operates in JRM (as shown in Fig. 10(b)). A qualitative comparison of the heating trends between the experimental parametric sweeps and the simulation was made. The simulation assumes a constant wall temperature along the resonance cavity. Consequently, the time-averaged heating power through the cavity tip is used as an analogue for tip temperature, allowing for comparison between experimental and simulated trends. Eq. (4) is used to determine the time-averaged heating power of the resonator tip for all nodes along the resonator wall where $x/L > 0.9$, which represents the section of the resonator expected to exhibit the highest wall temperature [31].

$$\dot{Q}_{x/L>0.9} = \int_{0.9}^{1.0} \pi D \bar{q} \; d\,(x/L) \tag{4}$$

Here $\bar{q}$ represents the time-averaged heat flux at a single node along the resonator wall and D the local diameter of the inner wall of the resonator. The time-averaged heating power is calculated by numerically integrating Eq. (4) over the relevant wall nodes. Fig. 13 shows the simulated heating power for both oxygen and nitrogen, computed at the same total temperature, total pressure, and NPR of the experimental sweeps. The simulated heating performance matches the measured temperature very closely in the case of nitrogen. The simulation accurately predicts the nozzle gap distance that yields the maximum temperature. The onset of significant resonance heating at $s/d_{throat} = 2$ is also evident in both experiments and simulations. Similarly, the steady decrease in heating beyond $s/d_{throat} = 3$ is captured by the simulation.

In the case of oxygen, both simulations and experiments consistently show a lower heating performance compared to nitrogen across all nozzle gap distances. The maximum heating power with oxygen is 11.3% lower than the maximum value attained with nitrogen, and the maximum temperature is reduced by 10.8%. The experiments with oxygen were performed at $p_t = 8.87$ bar, whereas the experiments with nitrogen were performed at $p_t = 10.2$ bar due to the difficulties in precisely setting the pressure on the regulator. Since a lower total pressure reduces the expected heating performance in JRM [10], this partly contribute to the observed differences in heating performance. In addition, the different thermodynamic properties of the two gases can further explain the reduced heating. Oxygen has a higher molar mass (32 g/mol versus 28 g/mol for nitrogen), which increases the gas density and increases the acoustic impedance of the resonator. In addition, its lower ratio of specific heats ($\gamma \approx 1.395$) compared to nitrogen ($\gamma \approx 1.404$ at 300 K), reduces the speed of sound and alters the resonance frequency. The lower speed of sound O_2 results in fewer heating cycles per second, leading to a lower rate of heat generation. Finally, oxygen's thermal conductivity is lower than that of nitrogen, which decreases heat transfer and contributes to reduced wall heating. The relative impact of these effects requires further investigation, which goes beyond the scope of this work.

It is also worth noting that the error bars in Fig. 13 for oxygen increase significantly after the point of maximum tip temperature. The reason for this is currently unknown, but a hypothesis can be made based on acoustic measurements. In Fig. 10(b) the spectra for O_2 show pronounced peaks below the dominant frequency at $s/d_{throat} = 3.25$ and 3.5. This could indicate that aside from the single shock wave entering the resonance cavity, additional pressure waves are present that are disrupting the regurgitant mode. The presence of these additional instabilities could explain the higher variation between experiments.

At the point of expected maximum heat generation, the numerical model deviates slightly from the trend seen in measured temperature. The simulation predicts the maximum heating power at $s/d_{throat} = 3.25$, as opposed to $s/d_{throat} = 2.75$ observed experimentally. Furthermore, the time-averaged heating power does not capture the steep drop seen experimentally $s/d_{throat} = 3.5$.

Despite these small mismatches, the simulations predict the experimentally observed heat flux and temperature trends quite well, demonstrating that the model captures the key physical mechanisms governing resonance heating and has good predictive capability.

6. Non-premixed ignition tests

The experiments with methane and oxygen aimed to investigate ignition via resonance heating using non-premixed fuel and oxidiser. A nozzle gap distance of $s/d_{throat} = 3$ was used for all combustion tests. A further set of resonance heating experiments was performed with O_2 at an NPR of 7.3 and an upstream total pressure of 16.6 bar. Compared

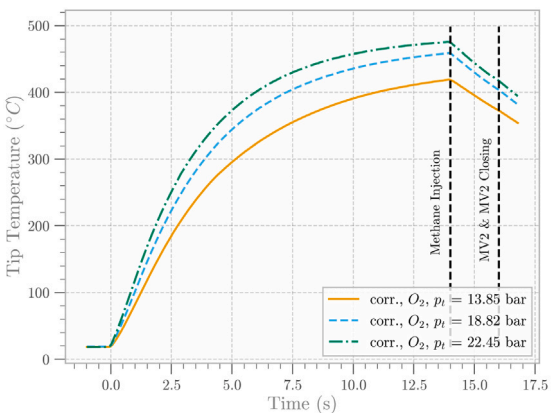

(a) Corrected temperature profile during three ignition attempts at varying oxygen upstream pressure.

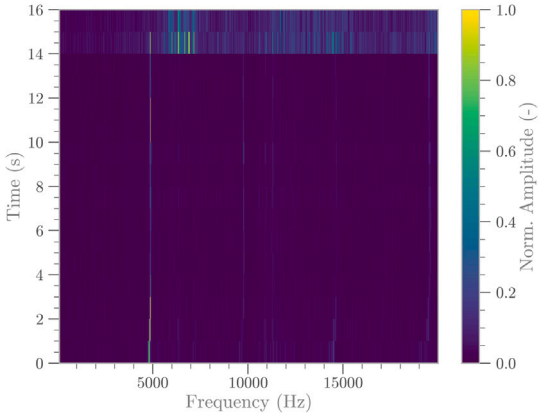

(b) Spectra plotted in one second intervals acquired during a oxygen resonance. Note that methane injection occurs at 14 seconds, followed by severe disruption of the resonance.

Fig. 14. Tip temperature and microphone spectra during an ignition attempt.

to the results shown in Fig. 13, the point of maximum heating shifted to $s/d_{throat} = 3$. The ignition tests were performed at similar NPR and upstream pressure, meaning that this optimal nozzle gap distance was used. Six ignition attempts were made, independently varying the upstream pressure of oxygen and methane The CGR set point at the methane and oxygen cylinder were adjusted between 14 and 23 bar. As a result, each test was conducted using a different mixture ratio and maximum cavity tip temperature. None of the ignition attempts were successful despite high cavity tip temperatures. The reasons for these ignition failures and the fundamental limitations of non-premixed designs are now discussed.

The equivalence ratio is a key parameter influencing both the ignition delay and auto-ignition temperature of the mixture [34]. Asaba et al. [35] reported ignition delays between 0.1 ms and 1.5 ms for mixtures of oxygen and methane, over a temperature range between 800 K and 2000 K and pressures between 3 bar and 7 bar. The shortest ignition delay occurred between $\phi = 1$ and $\phi = 1.3$ over this range. A short ignition delay is particularly critical for thermo-acoustic igniters due to the very short duration of each compression cycle in JRM.

All six ignition attempts fell within an equivalence ratio of $0.9 < \phi < 1.3$. This indicates that the global equivalence ratio inside the combustion chamber was within the range expected to provide short ignition delay and low auto-ignition temperature. However, the equivalence ratio at the cavity tip is not necessarily the same, as it depends on the local mixing of the propellants upstream of the cavity.

In all ignition tests, oxygen was used as the resonating gas, while methane was injected perpendicularly to the under-expanded jet. The flow of oxygen heated the resonator tip for 14 s, nearly reaching thermal steady-state. Methane was injected at T+14 s, while the oxygen was still flowing. At T+16 s, both main valves were closed, followed by a nitrogen purge. Fig. 14(a) shows the resonator tip temperature during three ignition tests with increasing oxygen total pressure. Resonance leads to a rapid temperature rise, with the cavity tip reaching up to 475.2 °C after 14 s at an oxygen total pressure of 22.45 bar. However, immediately after the methane is introduced, the tip temperature drops steadily. Fig. 14(b) shows spectra taken in second intervals during one ignition test. During resonance heating, a clear Jet Regurgitant Mode is visible. A slight shift in the fundamental frequency, from 4829 Hz to 4891 Hz, is visible between T+0 s and T+14 s, with the strongest variation at the start of the test. As the wall temperature of the resonance cavity increases, the gas temperature inside the cavity also increases, thereby raising the local speed of sound of the gas and shifting the resonance frequency upward.

Once methane is injected at T+14 s, the characteristic peak around 4900 Hz rapidly diminishes and disappears entirely at T+15 s. The methane injection appears to severely destabilise the acoustic resonance, effectively ending resonance heating, as shown in Fig. 14(a). Iwamoto defines two necessary conditions for sustaining JRM [23]. First, a low-pressure region must be present in front of the cavity inlet to enable a higher pressure differential between the under-expanded jet and the cavity entrance, providing strong inflow conditions for the next cycle. The more complete the evacuation of the cavity is, the larger the low-pressure region around the inlet of the cavity becomes at the end of the outflow phase. Then, a uniform pressure gradient in the mean flow direction is required in front of the resonator inlet, enabling uniform pressure recovery behind the under-expanded jet. Non-uniformities in a radial or tangential direction (relative to the mean flow) can severely distort the inflow into the cavity. Both of these conditions are disrupted by the high-speed flow of methane colliding with the resonating oxygen. This interference results in a sharp decrease in the cavity tip temperature once the methane is injected and disrupts the acoustic resonance inside the cavity, as shown in Fig. 14(b). Any further compression and expansion cycles in the cavity are disrupted, ending resonance heating. The oxygen-methane mixture entering the resonance cavity is no longer heated by the JRM, and the only remaining source of heat is the rapidly cooling resonator wall. Due to the low thermal inertia of the tip, this heat source is quickly exhausted. In addition, the oxygen and methane are likely not well mixed when entering the resonance cavity, so that the mixture at the tip is probably far from that of stoichiometric conditions. This, in turn, negatively affects both ignition delay and auto-ignition temperature, reducing the likelihood of ignition even further.

Although non-premixed operation was not successful in the present configuration, alternative injection strategies could be considered to enable safer ignition. Possible approaches include staged or pulsed injector, multi-port injection or partial premixing, which can improve the homogeneity of the mixture without compromising safety. Successful ignition of non pre-mixed oxygen and methane in a resonance igniter has been successfully demonstrated by Bauer and Haidn [12] in a configuration featuring coaxial fuel injection through the centre of a stem nozzle. The coaxial injection seems was shown to have little impact on the resonance behaviour of the driving gas while also ensuring the formation of combustible mixtures at the resonator tip. This demonstrates that gaseous fuel can be introduced without disrupting resonance in non-premixed when the injection strategy is carefully designed.

In comparison, the perpendicular injection of methane used in this study, despite easier to manufacture, disturbs the resonance frequency, limiting the likelihood of ignition. A potential improvement for the present igniter could be to reduce the injection angle of the fuel relative to the driving gas, thereby minimising disruption of the regurgitant mode while maintaining the inherent safety of non-premixed operation.

7. Conclusion

This study demonstrated that the experimentally-observed performance envelope and the switch in operating mode of a thermo-acoustic igniter can be accurately predicted by a numerical model. A test setup with exchangeable resonators and variable s/d_{throat} was designed and operated using oxygen and nitrogen as driving gases. Methane was injected in non-premixed conditions to examine the igniter's behaviour in such conditions. To identify the operating modes, a microphone placed outside of the cavity was used to monitor the acoustic signals, while thermocouples spot-welded to the tip of the resonance cavity measured the wall temperature. Resonance heating experiments were conducted using oxygen and nitrogen at different s/d_{throat} and upstream pressures. The parametric sweep with nitrogen demonstrated the switch from a Jet Screech Mode to a Regurgitant Mode. JSM was observed at gap distances lower than the predicted length of the first shock structure. Increasing s/d_{throat} beyond that point seemed to initiate JRM (at a nozzle pressure ratio of 6.8). Comparison with previous studies suggests that the onset of JRM is likely not universally defined by s/d_{throat} and NPR, but also depends on the cavity inlet geometry and surrounding combustion chamber configuration. Higher upstream pressures lead to a higher resonator tip temperature and a faster temperature rise in the pressure range of 14 bar to 23 bar.

Complementing these experiments, a numerical model of the acoustic resonance was developed using the Open Source CFD software SU2, providing additional insight into the system's behaviour. The simulations were performed on a fully structured grid. A mesh refinement study based on a grid convergence index and Richardson extrapolation showed low sensitivity of the flow density to mesh resolution. The wall heat flux, however, showed a much stronger dependence on mesh refinement despite achieving a good boundary layer resolution along the resonator walls. The Peng–Robinson equation of state, implemented in SU2, proved to be well-suited for predicting gas properties in the flow regime encountered inside the under-expanded jet and resonance cavity. The use of state-dependent specific heat capacities C_p and C_v was shown to be essential for accurately predicting wall heat flux during the JRM cycle.

This 2D axis-symmetric, compressible URANS simulation accurately predicts the switch from jet screech mode to the jet regurgitant mode. Extensive validation of the model was performed using a variety of s/d_{throat} using oxygen and nitrogen as driving gases. The predicted fundamental frequency showed an error consistently below 9.4%, with the lowest error at 2.6%. The model effectively identifies the combination of s/d_{throat} and NPR that lead to the highest rates of resonance heating, with the best agreement observed when nitrogen was used as the driving gas. The simulation approach employed in this study is computationally efficient, making it a valuable tool for the preliminary design of resonance igniters. The set point with the highest simulated heating power results from a longer flow dwell time due to a secondary pressure wave, rather than from the strongest incident shock wave. This phenomenon was only observed at $s/d_{throat} = 3$ and NPR = 6.8. This operating point provides a 9.8% increase in simulated heating power, which aligns with a 9% increase in the tip temperature measured experimentally.

Six ignition attempts were made with gaseous oxygen driving the resonance and gaseous methane as fuel, with equivalence ratios ranging between 0.9 and 1.3. None of the ignition attempts were successful. These failures highlight a fundamental limitation of non-premixed resonance igniter designs using gaseous fuels. The interaction between two high-speed gas flows of similar mass flow rates is found to disrupt the JRM and suppresses resonance heating. Premixed injection designs are therefore recommended when operating with gaseous fuels to maintain stable resonance and enable ignition.

CRediT authorship contribution statement

Jonathan Neeser: Writing – review & editing, Writing – original draft, Visualization, Validation, Software, Project administration, Methodology, Investigation, Formal analysis, Data curation, Conceptualization. **Francesca De Domenico:** Writing – review & editing, Supervision, Resources, Project administration, Methodology, Conceptualization.

Declaration of competing interest

The authors declare that they have no known competing financial interests or personal relationships that could have appeared to influence the work reported in this paper.

Appendix A. Supplemental material

The experimental data generated as part of this study, as well as the scripts used for data analysis are available on the 4TU.ResearchData archive under DOI: 10.4121/dbaa8f0f-59d2-4d58-8cc9-494af1b966f1.

Appendix B. Mesh refinement study

This appendix presents the mesh refinement study, which was conducted to assess the grid sensitivity of the numerical results. The discretisation of the domain means that the results obtained from the numerical model are inherently dependent on the grid resolution, which is especially relevant as shock waves are infinitely thin discontinuities in pressure, temperature, and velocity [22]. The local mesh resolution, and the order of the numerical schemes used to approximate convective fluxes, influence how well this discontinuity are resolved.

To ensure that the mesh used for these simulations provides a sufficiently accurate solution, a Grid Convergence Index (GCI) together with a Richardson extrapolation was employed [36]. The GCI quantifies the discretisation error in a local flow variable by comparing results across successively refined grids to an extrapolated value, which approximates the solution on an infinitely fine mesh.

The mesh was refined using a global mesh refinement parameter that also inversely scaled the mesh stretch factor. The number of elements in the gap between the nozzle and the resonator was also scaled with increasing s/d_{throat}. Since the flow inside the resonator is predominantly one-dimensional advection and aligned along the x-axis., the mesh refinement study was conducted with a constant Courant number, according to Eq. (B.1). This means that the time step was reduced proportionally with increasing spatial resolution:

$$C = \frac{u\Delta t}{\Delta x} \tag{B.1}$$

where u is the velocity in x-direction, Δt is the time step, and Δx is the mesh spacing. The study of the grid convergence index (GCI) and Richardson extrapolation were performed for a normalised grid spacing of 0.64, 1, 1.56, corresponding to 40%, 100% and 240% of the nominal number of nodes. As the simulation is unsteady, the parameters used for this analysis are time-averaged values sampled at discrete locations along the centreline and the wall of the resonance cavity. At each mesh refinement level, the simulation was run for three full JRM flow cycles. Fig. B.15 shows the mesh refinement study performed for fluid density and heat flux at three points along the length of the resonance cavity. The error bars represent the GCI at that refinement factor, with an additional 25% margin applied to the error [36]. The extrapolated

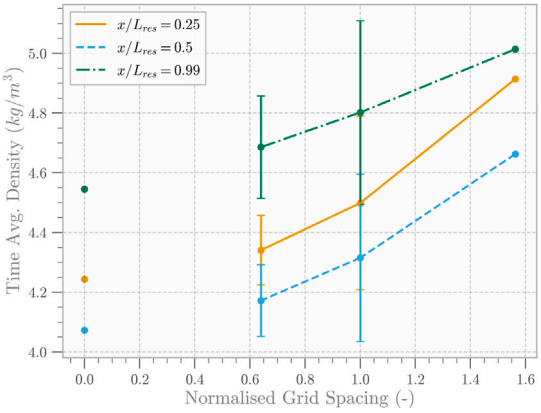

(a) Mesh refinement GCI and Richardson extrapolation for time average density at different resonator locations.

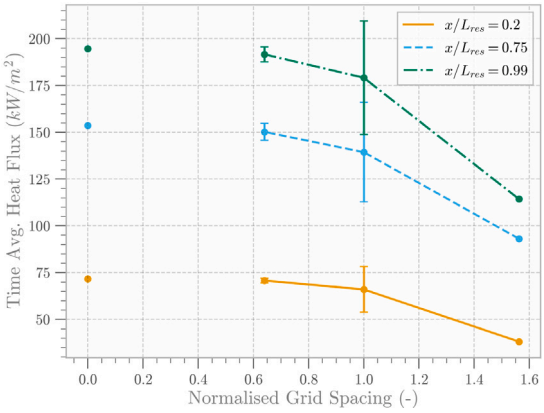

(b) Mesh refinement GCI and Richardson extrapolation for time average heat flux at different locations along the resonator wall.

Fig. B.15. Mesh verification.

values at a normalised spacing of 0 represent the estimated solution on an infinitely fine mesh.

Fig. B.15(a) shows a consistent GCI error of between 6.4% and 6.5% at the three locations along the resonator centreline. All points also show an apparent convergence towards the extrapolated value. The estimated p-factor in Fig. B.15(a) varies between 1.3 and 2.1. This value represents the order of convergence of the method and is expected to be ≤1 for a first-order convective scheme. The high p-factor observed here results from the constant Courant number and the use of a second-order method in time. As such, the p-factor does not directly represent the order of convergence of the spatial discretisation, but a combination of the spatial and time discretisations.

Fig. B.15(b) shows a mesh refinement study performed at three points along the resonator wall based on local heat flux. Here, the GCI error bar is still rather large at the nominal mesh spacing. Despite $y^+ < 1$ along the resonator at this mesh spacing, the estimate of wall heat flux still varies by almost 15 kW/m^2 between it and the finest mesh. This represents a GCI error of 16.9%. For this study, the error shown in Fig. B.15(b) is deemed acceptable, as only the relative differences in heat flux at different s/d_{throat} are considered (as opposed to any absolute estimate of the heat flux). For a numerical study interested in the absolute heat flux or wall temperature, a finer mesh, closer to 200% of the nominal number of nodes, is recommended.

Data availability

Experimental data associated with this paper can be found at DOI: 10.4121/dbaa8f0f-59d2-4d58-8cc9-494af1b966f1.

References

[1] Sutton GP. Rocket propulsion elements. 9th ed.. Hoboken, New Jersey: John Wiley & Sons Inc; 2017.

[2] Malm J. Inclusion of substances of very high concern in the candidate list. Helsinki: European Chemicals Agency (ECHA); 2011.

[3] Nufer BM. A summary of NASA and USAF hypergolic propellant related spills and fires. Tech. rep. NASA/TP-2009-214769, NASA; 2009.

[4] Mustafi S, DeLee C, Francis J, Li X, McGuinness D, Nixon C, Purves L, Willis W, Riall S, Devine M, Hedayat A. Cryogenic propulsion for the titan orbiter polar surveyor (TOPS) mission. Cryogenics 2016;74:81–7. http://dx.doi.org/10.1016/j.cryogenics.2015.11.009.

[5] Marchan RA. Small-scale supersonic combustion chamber with a gas-dynamic ignition system. Combust Sci Technol 2011;183(11):1236–65. http://dx.doi.org/10.1080/00102202.2011.589874.

[6] Marchan R, Oleshchenko A, Vekilov S, Arsenuk M, Bobrov O. 3D printed acoustic igniter of oxygen-kerosene mixtures for aerospace applications. In: Proceedings of the 8th European Conference for Aeronautics and Space Sciences. Madrid, Spain, 1-4 July 2019. 2019, http://dx.doi.org/10.13009/EUCASS2019-238.

[7] Phillips BR, Pavli AJ. Resonance tube ignition of hydrogen-oxygen mixtures. Tech. rep., NASA; 1971, URL https://api.semanticscholar.org/CorpusID:94163327.

[8] Bauer C, Lungu P, Haidn OJ. Numerical study on a resonance ignition system. In: Proceedings of the 8th European Conference for Aeronautics and Space Sciences. Madrid, Spain, 1-4 july 2019. 2019, http://dx.doi.org/10.13009/EUCASS2019-360.

[9] Conrad EE, Pavli AJ. Resonance-tube igniter for hydrogen-oxygen rocket engines. Tech. rep., TM X-1460, NASA; 1967.

[10] Lungu P, Bauer C, Haidn OJ. Design aspects and characterisation of a resonance igniter for oxygen/methane in-orbit propulsion systems. In: Proceedings of the 8th European Conference for Aeronautics and Space Sciences. Madrid, Spain, 1-4 July 2019. 2019, http://dx.doi.org/10.13009/EUCASS2019-651.

[11] Lebedev M, Bocharova O. Self-oscillatory flow in the Hartmann resonator – numerical simulation. Int J Aeroacoustics 2020;19(1–2):119–54. http://dx.doi.org/10.1177/1475472x20905037.

[12] Bauer C, Haidn OJ. Design and Test of a Resonance Ignition System for Green In-Orbit Propulsion Systems, arXiv:https://arc.aiaa.org/doi/pdf/10.2514/6.2016-4688. URL https://arc.aiaa.org/doi/abs/10.2514/6.2016-4688, doi: 10.2514/6.2016-4688.

[13] Sarohia V, Back L. Experimental investigation of flow and heating in a resonance tube. J FluidMech 1979;(94).

[14] Duronio F, Villante C, Vita AD. Under-expanded jets in advanced propulsion systems—a review of latest theoretical and experimental research activities. Energies 2023;16(18):6471. http://dx.doi.org/10.3390/en16186471.

[15] E. Rakowsky VM. Fluidic explosive initiator. Fluid Q 1974;6(1).

[16] Dippold VF. Computational simulations of convergent nozzles for the AIAA 1st propulsion aerodynamics workshop. Tech. rep., NASA; 2014, URL https://api.semanticscholar.org/CorpusID:13997215.

[17] Kuttruff H. Acoustics. London [u.a.]: Taylor & Francis; 2007.

[18] Bell IH, Wronski J, Quoilin S, Lemort V. Pure and pseudo-pure fluid thermophysical property evaluation and the open-source thermophysical property library CoolProp. Ind Eng Chem Res 2014;53(6):2498–508. http://dx.doi.org/10.1021/ie4033999.

[19] Lieuwen TC. Unsteady combustor physics. Online-Ausg. ed.. Cambridge: Cambridge University Press; 2013, Includes bibliographical references and index. - Description based on print version record.

[20] Economon TD, Palacios F, Copeland SR, Lukaczyk TW, Alonso JJ. SU2: An open-source suite for multiphysics simulation and design. AIAA J 2016;54(3):828–46. http://dx.doi.org/10.2514/1.j053813.

[21] Vitale S, Gori G, Pini M, Guardone A, Economon TD, Palacios F, Alonso JJ, Colonna P. Extension of the SU2 open source CFD code to the simulation of turbulent flows of fuids modelled with complex thermophysical laws. In: 22nd AIAA computational fluid dynamics conference. American Institute of Aeronautics and Astronautics; 2015, http://dx.doi.org/10.2514/6.2015-2760.

[22] Anderson JD. Modern compressible flow. 3. ed., internat. ed.. McGraw-hill series in aeronautical and aerospace engineering, Boston, Mass. [u.a.]: McGraw-Hill; 2003.

[23] Iwamoto J. Necessary conditions for starting and maintaining a stable oscillatory flow in a hartmann-sprenger tube. In: Flow visualization IV. 1987, p. 507–12.

[24] Roe P. Approximate Riemann solvers, parameter vectors, and difference schemes. J Comput Phys 1981;43(2):357–72. http://dx.doi.org/10.1016/0021-9991(81)90128-5.

[25] Wang Z. A fast nested multi-grid viscous flow solver for adaptive cartesian/quad grids. In: Fluid dynamics conference. American Institute of Aeronautics and Astronautics; 1996, http://dx.doi.org/10.2514/6.1996-2091.

[26] Menter F, Kuntz M, Langtry R. Ten years of industrial experience with the SST turbulence model. Heat Mass Transf 2003;4.

[27] Menter FR. Performance of popular turbulence model for attached and separated adverse pressure gradient flows. AIAA J 1992;30(8):2066–72. http://dx.doi.org/10.2514/3.11180.

[28] Pope SB. Turbulent flows. 1st ed.. Cambridge [u.a.]: Cambridge Univ. Press; 2015, p. 727–48, Literaturverz. S..

[29] Sobieraj G, Szumowski A. Experimental investigations of an underexpanded jet from a convergent nozzle impinging on a cavity. J Sound Vib 1991;149(3):375–96. http://dx.doi.org/10.1016/0022-460x(91)90443-n.

[30] Bouch D, Cutler A. Investigation of a Hartmann-Sprenger tube for passive heating of scramjet injectant gases. In: 41st aerospace sciences meeting and exhibit. American Institute of Aeronautics and Astronautics; 2003, http://dx.doi.org/10.2514/6.2003-1275.

[31] Brocher E, Maresca C. Etude des phenomenes thermiques dans un tube de Hartmann-Sprenger. Int J Heat Mass Transfer 1973;16(3):529–38. http://dx.doi.org/10.1016/0017-9310(73)90221-4.

[32] Oliveira A, Avrit A, Gradeck M. Thermocouple response time estimation and temperature signal correction for an accurate heat flux calculation in inverse heat conduction problems. Int J Heat Mass Transfer 2022;185:122398. http://dx.doi.org/10.1016/j.ijheatmasstransfer.2021.122398.

[33] Bauer C, Hauser M, Haidn OJ. Investigation of stabilization effects in Hartmann-Sprenger tubes. Trans Jpn Soc Aeronaut Space Sci, Aerosp Technol Jpn 2016;14(ists30):95–100. http://dx.doi.org/10.2322/tastj.14.pa_95.

[34] Bounaceur R, Glaude P-A, Sirjean B, Fournet R, Montagne P, Vierling M, Molière M. Prediction of auto-ignition temperatures and delays for gas turbine applications. J Eng Gas Turbines Power 2015;138(2). http://dx.doi.org/10.1115/1.4031264.

[35] Asaba T, Yoneda K, Kakihara N, Hikita T. A shock tube study of ignition of methane-oxygen mixtures. Symp (Int) Combust 1963;9(1):193–200. http://dx.doi.org/10.1016/s0082-0784(63)80026-0.

[36] Celik I, Ghia U, Roache P, Freitas C, Coloman H, Raad P. Procedure of estimation and reporting of uncertainty due to discretization in CFD applications. J Fluids Eng 2008;130:078001. http://dx.doi.org/10.1115/1.2960953.